Measurement 203 (2022) 111930

Contents lists available at ScienceDirect

Measurement

journal homepage: www.elsevier.com/locate/measurement

Non-destructive system for in-wall moisture assessment of cultural heritage buildings

Magomed Muradov [a,*], Patryk Kot [a], Jakub Markiewicz [b], Sławomir Łapiński [b], Aleksandra Tobiasz [c], Katarzyna Onisk [c], Andy Shaw [a], Khalid Hashim [a], Dorota Zawieska [b], Ghulam Mohi-Ud-Din [a]

[a] Built Environment and Sustainable Technologies Research Institute (BEST), Liverpool John Moores University, Byrom Street, Liverpool L3 3AF, United Kingdom
[b] Faculty of Geodesy and Cartography, Warsaw University of Technology, Pl. Politechniki 1, 00-661 Warsaw, Poland
[c] Documentation and Digitalization Department, Museum of King Jan III's Palace at Wilanów, ul. Stanisława Kostki Potockiego 10/16, 02-958 Warsaw, Poland

ARTICLE INFO

Keywords:
Cultural Heritage
Microwave Sensors
Moisture Content
Non-destructive Testing
Photogrammetry
Structural Health Monitoring

ABSTRACT

Cultural heritage sites are exposed to several factors that cause their deterioration and degradation, namely moisture content. There are several destructive and non-destructive methods available to monitor moisture. However, destructive methods are avoided in cultural heritage to prevent surface damage, while non-destructive methods are limited to penetration capabilities. This study proposed geo-positioning of non-destructive moisture assessment based on microwave spectroscopy and close-range photogrammetry. The experimental data were collected at the Museum of King Jan III's Palace at Wilanów, Poland. The data was analysed using clustering algorithms (*t*-SNE, PCA, K-Means and Hierarchical), which demonstrated clear clusters. However, the microwave results did not fully align with the pin-type moisture data as the proposed microwave system was able to penetrate through the material, whereas the pin-type meter only measured the surface. Therefore, the microwave sensing approach provided more detailed moisture information of the measured material.

1. Introduction

Cultural heritage (CH) is an integral part of modern society that allows to observe and analyse the past, and it is a crucial part of cultural, environmental, social and economic sustainability [1]. Therefore, the sustainable management of cultural heritage buildings in the 21st century is an essential strategical element for the European Union [2]. In addition, it stated in 'European Framework for Action on Cultural Heritage' [3] that safeguarding and preservation of CH is not only a national competence, but it is also an EU responsibility as set out in the founding Treaties. Recently, digital technologies have been utilised in CH as they offer unprecedented opportunities for the improvement of public access to CH assets and in their curation and re-use. Moreover, researchers have been implementing digital technologies in various aspects of the safeguarding and preservation of CH. For instance, numerous research studies have been undertaken to develop accurate, complete, and multi-source digital documentation of cultural heritage objects and sites for in-depth Structural Health Monitoring (SHM) analysis [4,5,6]. This is particularly important in the context of the adequate registration and documentation of objects as well as for object degradation analysis. For this purpose, the image-based (passive methods such as close-range photogrammetry, Structure-from-Motion/Multi-View Stereo or Remote Sensing techniques) [7,8,9] as well as range-based (passive methods, i.e. Terrestrial Laser Scanning) methods are used for 3D shape reconstruction and physical information about the object determination [10,11,12]. Integrating these techniques to complement each other and provide multi-source data for in-depth structural health analysis and detailed cultural heritage architectural documentation is essential. Over the past decades, the degradation of CH due to exposure to atmospheric and water pollution has become an increasing concern [13]. Therefore, it is vital to address the continuous deterioration of heritage structures due to the appearance of different defects caused by ageing, unpredicted events, environmental conditions, and incorrect previous restoration treatments [14].

---

* Corresponding author.
E-mail addresses: M.Muradov@ljmu.ac.uk (M. Muradov), P.Kot@ljmu.ac.uk (P. Kot), jakub.markiewicz@pw.edu.pl (J. Markiewicz), slawomir.lapinski@pw.edu.pl (S. Łapiński), A.Shaw@ljmu.ac.uk (A. Shaw), K.S.Hashim@ljmu.ac.uk (K. Hashim), dorota.zawieska@pw.edu.pl (D. Zawieska), g.mohiuddin@ljmu.ac.uk (G. Mohi-Ud-Din).

https://doi.org/10.1016/j.measurement.2022.111930
Received 8 June 2022; Received in revised form 6 September 2022; Accepted 7 September 2022


(a)
(b)
(c)
(d)
(e)

Fig. 1. Museum of King Jan III's Palace at Wilanów. (a) Front of the Palace with the marked south gallery, (b) The map of the Palace with the marked south gallery, (c) the photo of the gallery interior, (d-e) Fragments of the orthoimages of the tested walls.

Environmental conditions introduce new challenges in the protection and conservation of CH, namely monumental complexes, archaeological sites, and historic buildings are at risk as a consequence of the impacts of slow and extreme environmental changes, particularly in urban areas, where the effect of multiple pressures is amplified [15]. The extreme changes in temperature, relative humidity and wind have a negative impact on the cultural heritage materials, which with increased changes in the frequency and intensity of severe weather events, will negatively impact the biological, chemical, and physical mechanisms, causing the degradation of the cultural heritage sites [16,17,18].

Most CH sites are constructed using porous material (e.g., ceramic bricks), prone to damp rise. The rising damp is a phenomenon where the water moves upward by capillary forces within the porous material. The most common cause of moisture is faulty waterproofing of foundations or its complete absence. These defects can lead to long-term dampness of the walls, which in turn attracts fungi, microorganisms, and moulds that are harmful to health [19]. Thus, water is considered an enemy to CH. The locating, measuring, and removing moisture from masonry surfaces and structures is an essential part of any CH conservation work, which has become a standard routine for conservators. These activities include (1) continuous monitoring of the moisture presence during seasonal cycles, (2) measuring the moisture level and identifying the individual damage thresholds of specific decorative elements such as mural paintings and stuccoworks and (3) removing the excess moisture using the appropriate techniques to maintain the balance between the effectiveness and invasiveness of the selected method [20].

Non-destructive measurement techniques are the preferred assessment methods in cultural heritage monitoring, as damages can be detected at the early stages, and specific actions can be taken to preserve the measured object [21]. The early detection of anomalies enhances cultural heritage maintenance and prevents the decay or loss of characteristic structures or the need for costly and extensive restoration [22]. Martínez-Garrido *et al* [23] published a comprehensive study for moisture control in cultural heritage using several non-destructive techniques, which included Electrical Conductivity meter (EC) [24], Infrared Thermography (IRT) [21,25,26], Electrical Resistivity Tomography (ERT) [19,27,28,29] and Ground-Penetrating Radar (GPR) [30,31] techniques to provide sub-surface and surface information. Two approaches were investigated using these techniques, namely (1) a surface/sub-surface measurement using a combination of EC and IRT and (2) an in-wall measurement using ERT and GPR techniques. The EC and IRT methods were assessed to determine the distribution of dampness on walls and to define the most intense moisture on the surface of the measured walls. The EC meters are specifically designed for moisture assessment of wood; however, they are also widely used for estimating the degree of moisture in surfaces with various construction materials (such as plaster, cement, and stone). The IRT technique [14] is also used for surface measurements based on images representing infrared radiation emitted by objects. The downside of these methods is being limited to the surface measurement of construction materials, whereas an in-wall measurement is crucial in order to characterise moisture issues and their origin within a structure. The in-depth moisture content

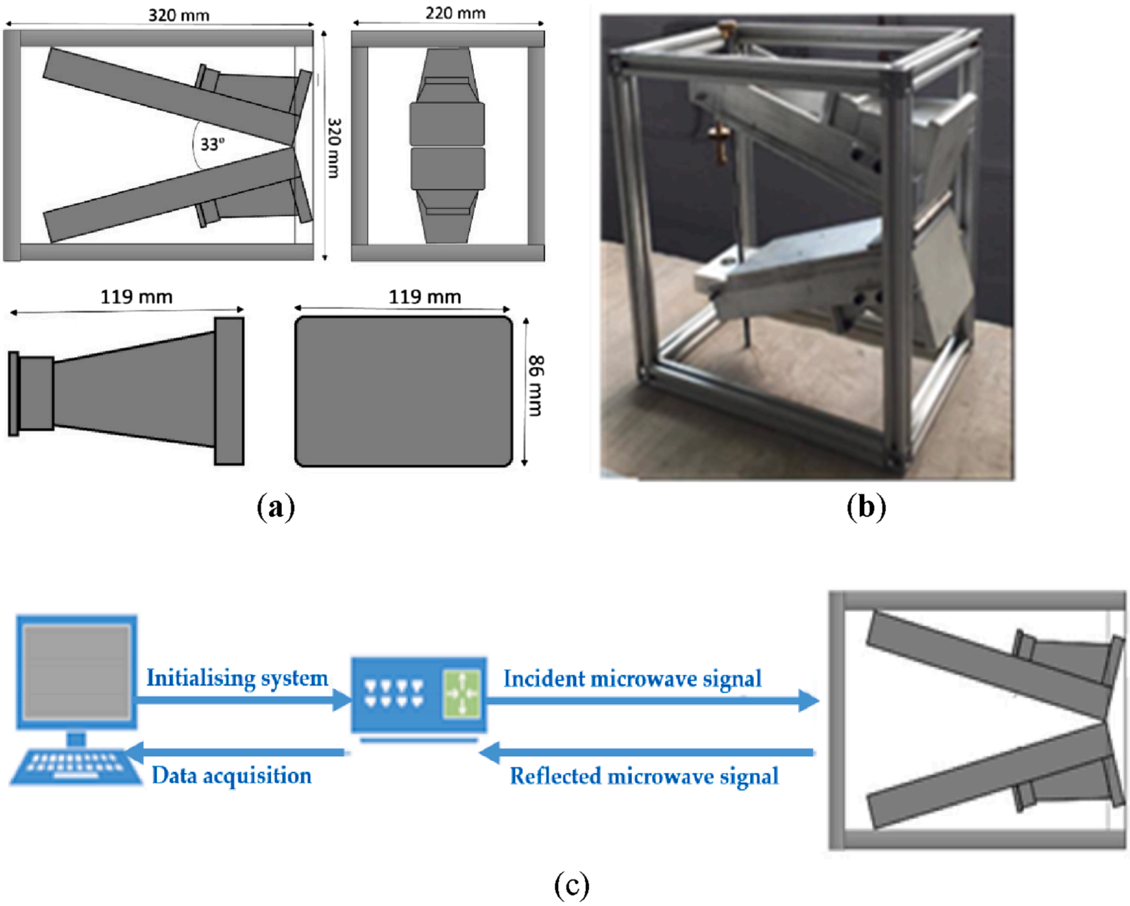

Fig. 2. (a) Sensor dimensions, (b) Proposed microwave Transmitter/Receiver setup and (c) block diagram of proposed Sweep Frequency system for SHM [43].

measurements within the wall structures were assessed using the ERT and GPR techniques. The ERT only estimates the sub-surface resistivity distribution from the surface measurements, whereas the GPR technology is able to penetrate much deeper into a construction material.

Furthermore, researchers studied microwaves [32,33] to determine moisture in building structures owing to the technique's ability to penetrate through building materials. Kot *et al.* [34,35] investigated microwaves as a non-destructive approach for monitoring excess moisture and membrane failure within concrete structures. The microwave approach demonstrated the ability to monitor the anomalies in concrete structures, namely penetrating through concrete specimens, determining excess moisture and failure of membrane layers. The penetration capability was also demonstrated by ultrasonic technique [36] in concrete. However, the referenced method required access to both sides of the tested sample, which is not always possible in cultural heritage sites. Thus, the microwave technique was selected as the moisture monitoring method (for in-wall measurement aspect of the study) for this investigation.

In this work, a novel multispectral system (comprised of microwave, photogrammetry and Terrestrial Laser Scanning technologies) is introduced to (1) identify in-wall moisture content and (2) provide its precise location (geo-positioning in space) on the measured wall as a part of detailed architectural documentation for safeguarding and preservation of cultural heritage buildings [37]. The existing geo-positioning (in space) techniques were investigated, and a new methodology for positioning the multispectral system was proposed by Markiewicz *et al.* [38], which will be evaluated in this article at the Museum of King Jan III's Palace at Wilanów, described in Section 2.

2. Materials and methods

The initial stage of this study was undertaken in the Museum of King Jan III's Palace at Wilanów (Fig. 1), particularly in the Open Gallery/Transparent Garden Gallery, which was added during the extension of the chateau in 1681–1683. The south gallery originally had 4 bays and was extended by 2 more bays in the first third of the 18th century to close the tower from the south. There are eighteenth-century landscape frescoes on the gallery walls and ceiling. The gallery walls' moisture content is monitored weekly using a Gann Hydromette UNI 2 moisture meter with the B50 active electrode. However, the penetration depth of the measurement is limited to the surface of the wall and a single-point measurement; therefore, the meter does not provide adequate moisture measurements of the walls.

2.1. *Principle of microwaves for moisture measurement*

In order to obtain the in-wall measurements of the moisture content, microwave spectroscopy was utilised. Microwaves can propagate through the dielectric material and interact with the material to produce information about this material. Materials will have different properties, which will influence the degree of the microwave interaction with these materials, which can be determined by the permittivity of the material. Relative permittivity ε_r is in a complex form in microwave frequency ranges and is presented in Eq. (1) [39].

$$\varepsilon_r = \varepsilon_r' - j\varepsilon_r'' \tag{1}$$

where ε_r' and ε_r'' are the real part and the imaginary part of the relative permittivity, respectively.

The electric field of a travelling wave *E(x)* in a material is expressed

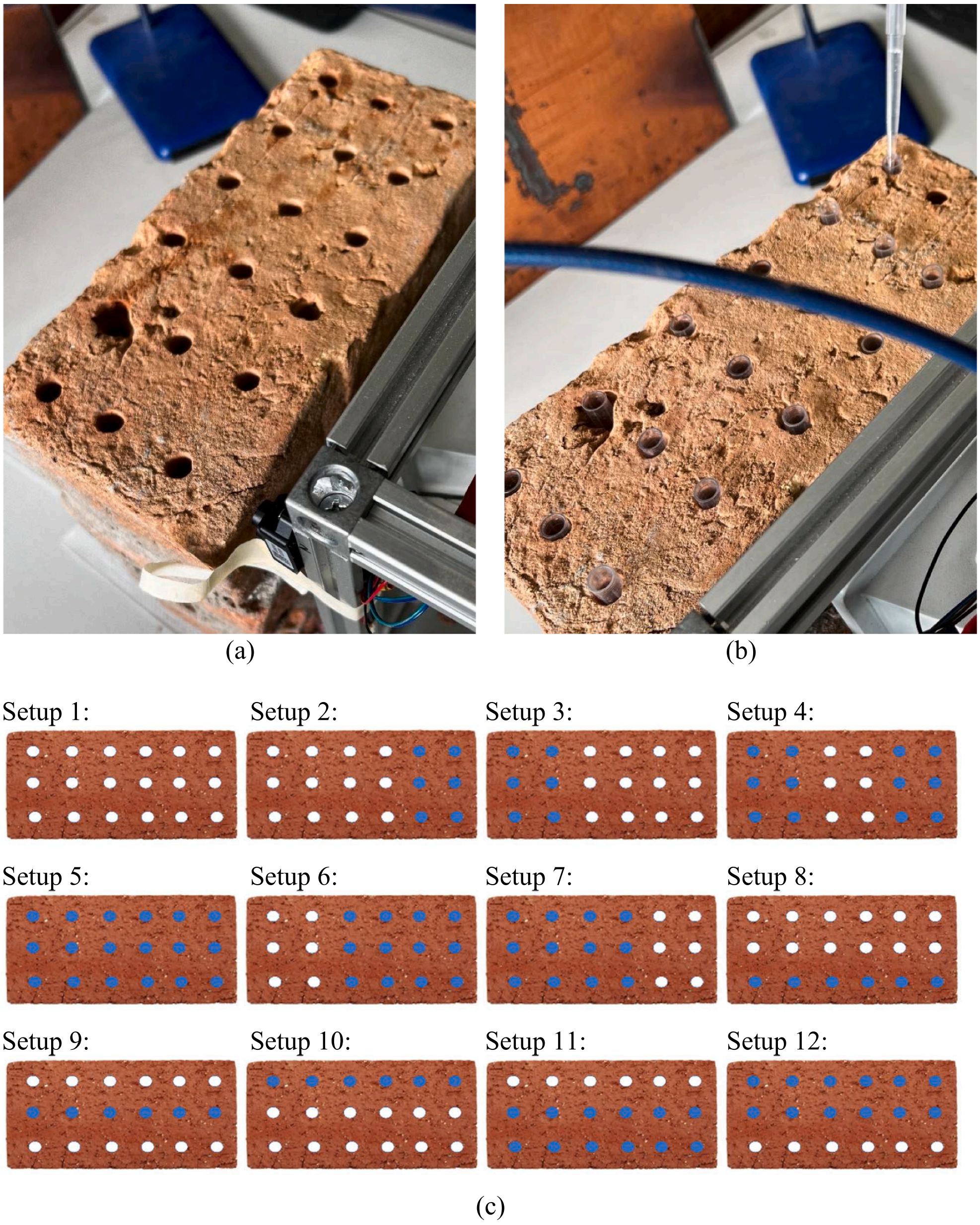

Fig. 3. Laboratory-based brick setup.

using the permittivity as follows:

$$E(x) = E_0 \exp(-k''x).\exp(-jk'x) \quad (2)$$

where

$$k' = k_0 Re(\sqrt{\varepsilon}), \quad k'' = k_0 Im(\sqrt{\varepsilon}$$

and

$$k_0 = \frac{2\pi}{\lambda_0}$$

where λ_0 is a wavelength in vacuum, and E_0 is an intensity of the electric field.

When the condition of permittivity is $\varepsilon'^2 \gg \varepsilon''^2$, the electric field is expressed as follows:

$$E(x) = E_0 \exp\left(-\frac{\pi}{\lambda}.\frac{\varepsilon''}{\sqrt{\varepsilon'}}x\right).\exp\left(-j\frac{2\pi}{\lambda}\sqrt{\varepsilon'}x\right) \quad (3)$$

Eq. (3) demonstrates that the phase depends on ε', whereas the intensity of the electric field depends on both ε' and ε''. On the other hand, the phase will also depend on both ε' and ε'', if the condition of $\varepsilon'^2 \gg \varepsilon''^2$ is not met. Therefore, the in-wall measurement of moisture can be determined via the intensity or the phase of the wave as the permittivity of the material is a function of the moisture since the permittivity of water (70–80) is greater than almost all materials, which significantly affects the microwave signal [39]. Furthermore, the field penetration into materials can be determined by the skin depth calculation, i.e., the depth at which the transverse electric and magnetic fields decay to $1/e$ of their amplitudes upon values entering the surface. The calculation is undertaken using the loss tangent and real part of the permittivity of the material [40]. The loss tangent of a material is expressed by the following Eq. (4):

$$\tan\delta = \frac{\varepsilon_r''}{\varepsilon_r'} \quad (4)$$

While the skin depth of a material is expressed with:

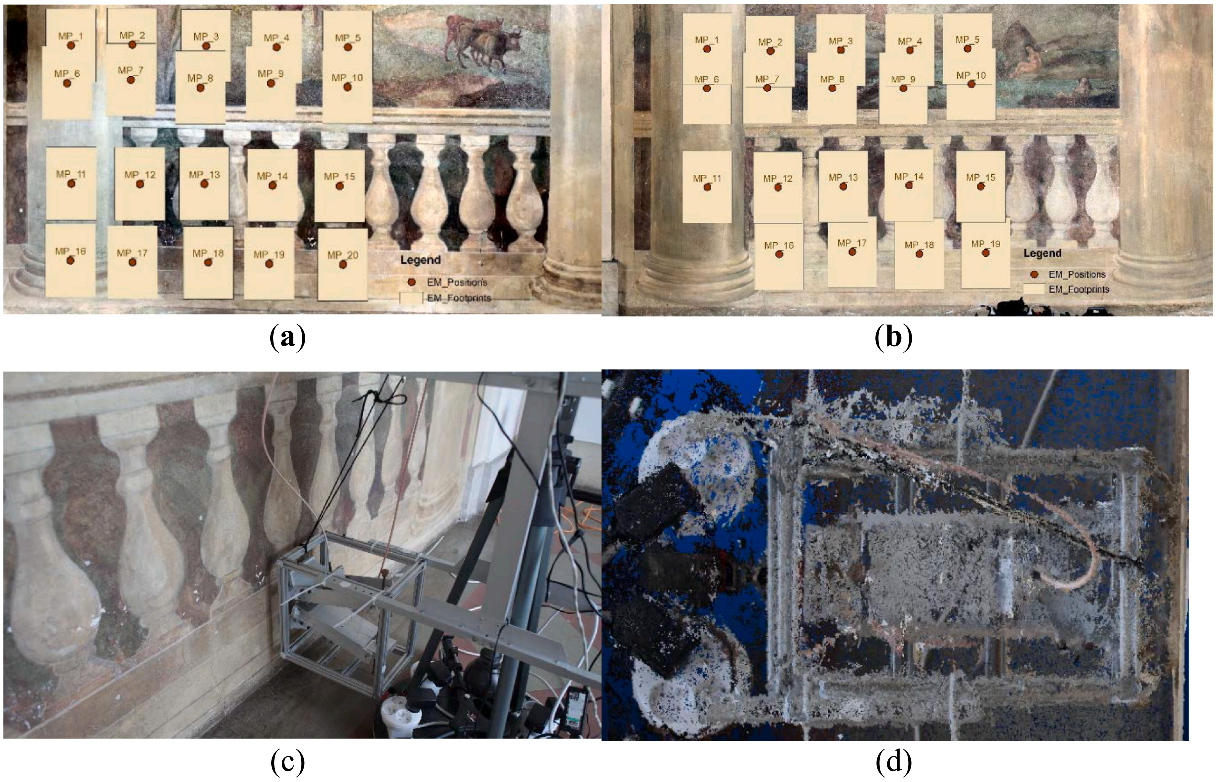

(a) (b) (c) (d)

Fig. 4. Microwave system positions sketch with marked sensors footprints for (a) Test Site I and (b) Test Site II, (c) The example of the measurement setup, (d) Top-view of the sensor's location near the investigated wall.

$$\sigma_s = \frac{1}{\alpha}[m] \tag{5}$$

Where α is the attenuation constant given by.

$$\alpha = \frac{\omega}{c\sqrt{2}}\sqrt{\varepsilon_r' \mu_r'}\sqrt{\sqrt{1+tan^2\delta}-1} \tag{6}$$

Where c is the speed of light, ω is the angular frequency and relative permeability μ_r' is set equal to 1 for concrete.

Pisa *et al.* [41] reported brick measurements in the 1.7 GHz – 18 GHz frequency range that demonstrated permittivity values between 3.7 and 4.6 for the real part and 0.12 and 0.6 for the imaginary part, respectively, were used for the calculation of the skin depth. Based on the calculations, the skin depth ranges from 90 cm to 2 cm in the frequency range between 1.7 GHz and 18 GHz. The proposed microwave system enables (1) the adjustment of the angle between the transmitter and receiver and (2) frequency sweep (the operational frequency range of the used horn antennas is 2–18 GHz) to focus on the particular area of the measured material and avoid interference from the external environment.

2.2. Laboratory study of the proposed microwave system

An assessment of the microwave (MW) system's suitability to detect moisture inside walls was conducted in a laboratory environment at Liverpool John Moores University. The MW horn antenna system (Fig. 2) consisted of two wideband horn antennas [42] (a receiver and a transmitter), Rohde & Schwarz ZVL13 Vector Network Analyser (VNA) and a laptop with a bespoke LabVIEW data acquisition program. The measurements were taken via S-parameter (S_{21}) within the frequency range of 2–13 GHz and 4000 sweep points. The incident microwave signal is sent via the transmitter antenna, and the reflected microwave signal of the measured object is captured via the receiver antenna. The data was recorded in the complex data format, which can be converted to the magnitude and phase of the captured signal for further analysis.

The study used red bricks with 18 drilled holes 10 mm each (see Fig. 3a). Plastic tubes were inserted into each hole (see Fig. 3b), and baseline measurements (S_{21}) were taken with the system. All the measurements were replicated three times in this study. Once the baseline measurements were captured, various setups (see Fig. 3c) were configured, i.e., multiple holes were filled with water (2 mL per hole), and S_{21} measurements for each setup were recorded via VNA. Each setup represented potential water distribution within walls. In this experiment, the moisture meter did not present any variation in the water content; therefore, this data is not included in the analysis. This investigation will provide an understanding of how the system will react to set water distributions within the brick wall, which is essential for the analysis of the carried out experimental work at the museum as the in-wall measurements are not possible due to the requirement of the non-destructive methods, i.e., the microwave measurements at the museum will not be accompanied with the quantifiable in-wall water content measurements.

2.3. Case study at Museum of King Jan III's Palace at Wilanów

The experimental work comprised measurements with the MW system (Fig. 2), a pin-type moisture meter and a photogrammetry setup on selected walls in the palace. The MW system was pointed at the wall and positioned approximately 2–3 cm from it (Fig. 4). The data acquisition methodology was followed from the laboratory study (Section 2.2). Prior to the MW measurements, the moisture content of measured positions on both Test Sites was recorded using a pin-type moisture meter. In addition, photogrammetry measurements were taken via the Canon 5D Mark II camera and Z + F 5006 h laser scanner.

The proposed method for processing data from the multi-sensor platform (Fig. 4) is a multi-stage process based on the combination of the commonly used algorithms in Computer Vision (such as Structure-from-Motion, MultiView-Stereo for close-range image processing), Terrestrial Laser Scanning point cloud processing and Electromagnetic

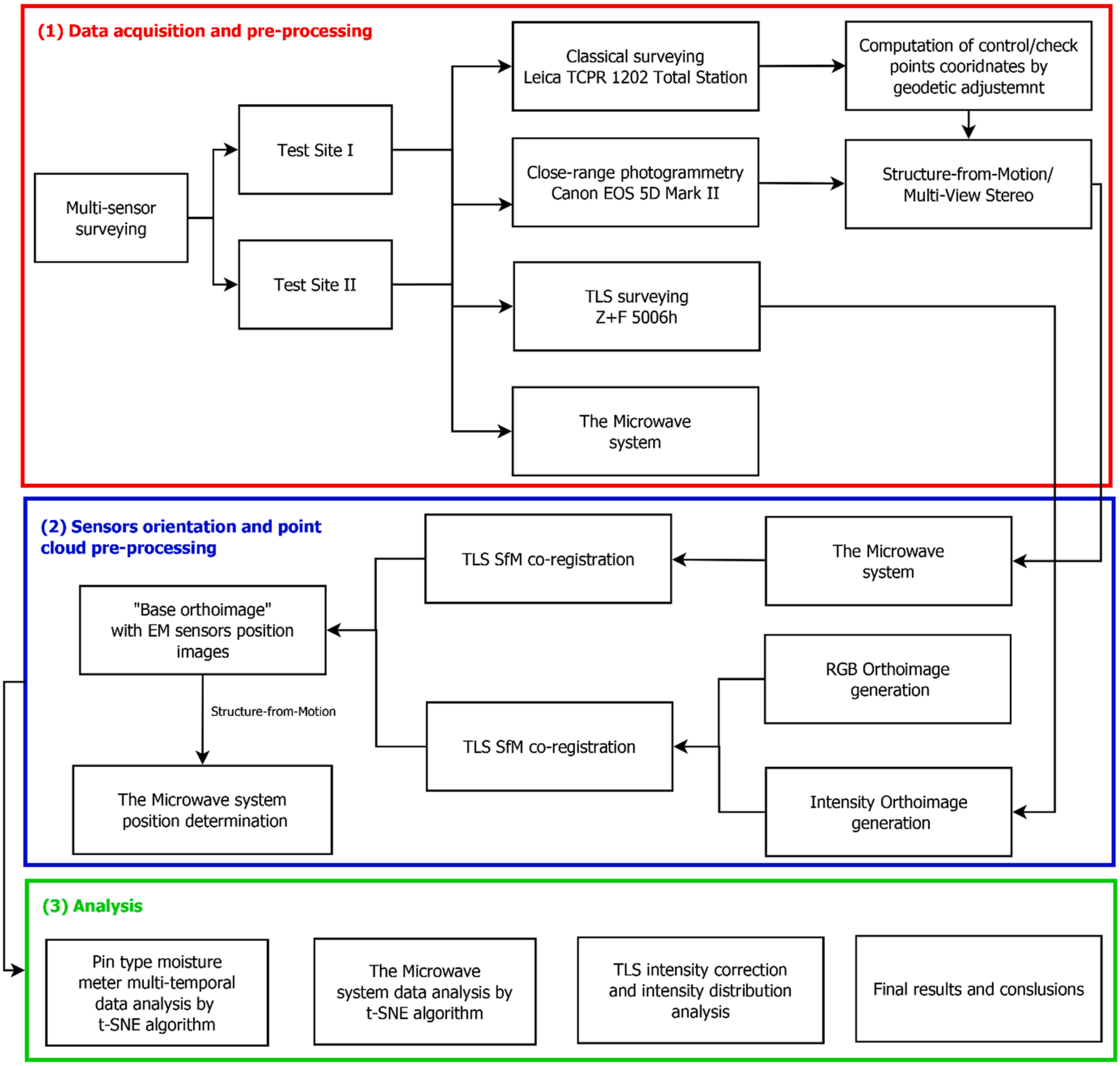

Fig. 5. The diagram of the performed experiments: data acquisition, processing and analysis.

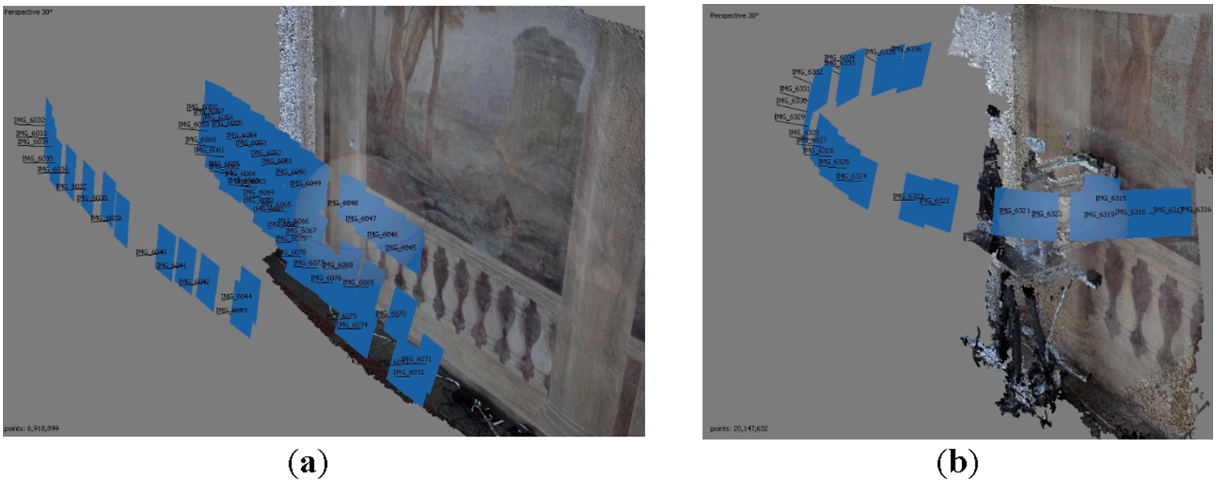

Fig. 6. Schematic of the image taking used to (a) generate the reference orthoimage and (b) determine the position of the MW system in space.

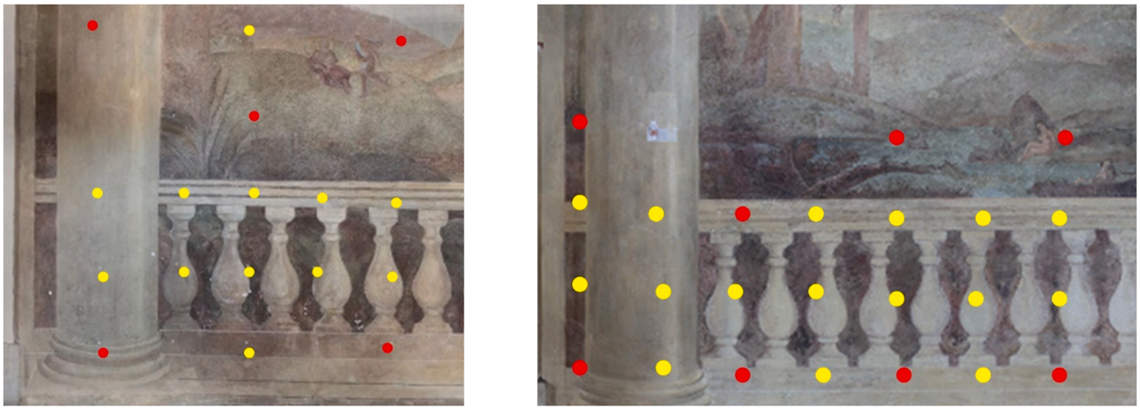

(a) (b)

Fig. 7. The sketch of reference point distribution used for image orientation with natural points measured by Total Station (control points – red, check points – yellow) for (a) Test Site I and (b) Test Site II.

Data pre-processing and interpretation. The proposed data processing and integration is a novel approach allowing orientation and integration of results from different-range and wavelength sensors. The detailed diagram of the data processing is shown in Fig. 5.

(1) The first stage of multi-source processing involves the measurement of the coordinates of photogrammetric network points using the classical tacheometric method (TS). Coordinates of natural unsigned details of wall paintings were determined using the adjustment of TS measurements acquired with the spatial resection method from two TS positions.

(2) The obtained close-range images were processed for two purposes: (1) for "orthoimage generation" (see Fig. 6a) to create documentation from the multi-sensor platform data. All data processing was compleated using Agisoft Metashape software [44], resulting in a dense point cloud, a Numerical Object Surface Model and an RGB orthoimage. Natural control points were used to fit the images into the adopted reference system, bundle adjustment check points were used to assess the accuracy of the process, and (2) the images were also used to orient the Microwave (MW) system (see Fig. 6b) to the assumed reference system. Markiewicz *et al.* [38] present a detailed description of the algorithm.

(3) The processing of point clouds from terrestrial laser scanning for orthoimages generation was processed according to the methodology proposed by Markiewicz *et al.* [46]. The only change to the proposed method was the correction of raw intensity based on surface normal angles and scanning distance according to the methodology proposed by Fang *et al.* [45].

(4) The co-registration of point clouds acquired from terrestrial laser scanning and close-range images (TLS-SfM approach) was carried out using the feature-based registration method proposed by Markiewicz *et al.* [46]. The corresponding points were detected by the SURF algorithm [47] implemented in the author's software.

(5) The captured complex MW data was converted into magnitude format to determine the microwave energy absorption level by the moisture within the measured walls. The magnitude data consisted of 4000 points, swept across the frequency range of 2–13 GHz, i.e., the amplitude changes at various frequencies were recorded.

(6) To visualise and find the clusters of the data, which share similar characteristics in terms of moisture content, the data has been analysed using the *t*-Distributed Stochastic Neighbour Embedding (*t*-SNE) algorithm.

Table 1

The quality assessment of the images' orientation used for orthoimages generation.

Test Site	Parameter	Point type	reprojection error [pix]	X [mm]	Y [mm]	Z [mm]	L [mm]
I	Minimum	Control points	0.4	−0.5	−1.7	−2.3	1.0
	Maximum		0.5	0.4	1.6	2.4	4.2
	Mean		0.4	0.4	0.8	2.4	2.7
	Median		0.4	0.0	0.0	1.3	2.4
	RMSE		0.4	0.4	1.1	1.6	2.9
	Minimum	Check points	0.3	−0.5	−1.2	1.4	1.9
	Maximum		0.5	0.0	0.8	2.5	2.7
	Mean		0.4	0.2	0.1	1.9	2.2
	Median		0.4	−0.1	0.8	0.5	2.0
	RMSE		0.4	0.3	1.0	1.0	2.2
II	Minimum	Control points	0.1	0.3	−3.3	−3.3	1.0
	Maximum		0.6	−0.6	2.1	3.3	4.0
	Mean		0.3	0.1	0.6	1.2	3.1
	Median		0.4	0.0	0.0	1.0	2.8
	RMSE		0.4	0.2	1.6	1.6	3.3
	Minimum	Check points	0.5	−1.1	−2.0	−3.4	1.4
	Maximum		0.7	1.5	3.4	3.5	4.4
	Mean		0.4	0.6	1.6	1.6	3.5
	Median		0.3	0.5	1.0	1.3	3.0
	RMSE		0.5	0.7	1.9	1.9	2.6

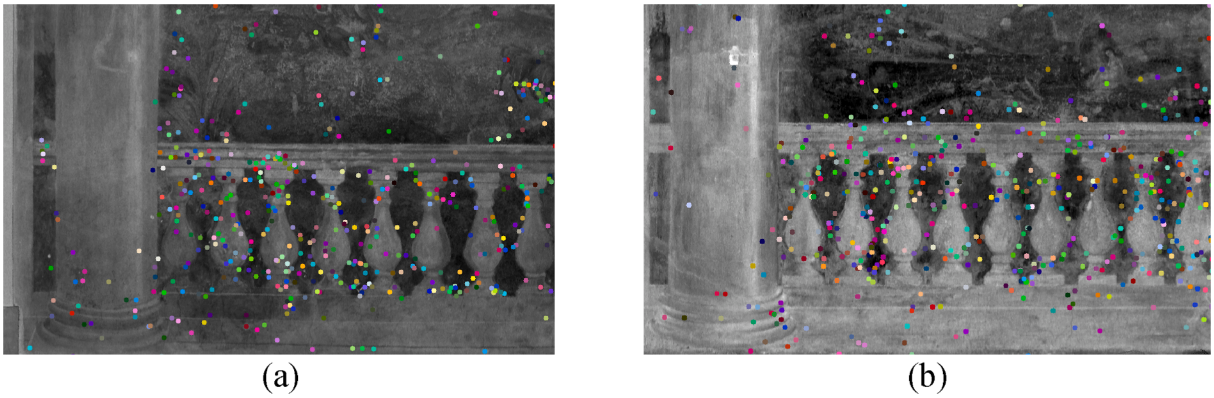

Fig. 8. The sketch of the points distribution automatically detected and matched by SURF algorithm on RGB and TLS orthoimages for (a) Test Site I and (b) Test site II.

3. Results and discussion

3.1. *Surveying data acquisition and processing*

The initial acquisition process was divided into two main parts: (1) Total Station measurements with a Leica TCRP 1202 with angular accuracy of 2 *sec*., linear accuracy of 2 mm + 2 ppm for photogrammetric network design and (2) TLS data acquisition with resolution 6.1 mm/10 m.

The total station acquired data from 2 measurement stations and at 2-time series to ensure the data's accuracy, reliability, and removal of errors. In the last square adjustment process, the mean square errors of determining the position for natural points (in 3D space) do not exceed 1.5 mm.

TLS point clouds were obtained from 2 separate stations positioned parallel to the object with a maximum distance of 3 m. In the pre-processing step, point clouds were filtered by the intensity and down-sampled to the 1 mm resolution. These point clouds were used to generate the intensity orthoimage by the methodology proposed by Markiewicz *et al.* [46].

3.2. *Image orientation for "base orthoimage generation"*

The first stage of multi-source data processing involved the generation of reference point cloud and orthoimage with the depth map, which has been used for a co-registration of the MW system's positions. Both approaches based on (1) unsignalised details (points) measured with Total Station, and (2) automatically detected tie points on point clouds from Terrestrial Laser Scanning were analysed to assess the suitable method for reference point cloud registration.

3.2.1. *The "classical" SfM based on the control and check measured by the total station*

Natural reference points were divided into control points, used to build a mathematical model and determine orientation parameters, and control points, used for independent quality assessment. Fig. 7a and b show the distribution of points measured by Total Station on the orthoimages for Test Site I and II.

In both cases, the distribution of scores was similar for both test fields because measured points were used for fitting in and checking the photographs' orientation not only for generating the reference orthoimage but also for orienting individual groups of images of each MW system's position. Table 1 shows the results of the bundle adjustment process for images obtained in Scenario I. The minimum, maximum and mean values were used to evaluate the quality of the images' orientation. Additionally, the Root Mean Square Error (RMSE) (Eq. (7)) were compared to determine the outliers of the obtained datasets.

$$\mathrm{RMSE} = \sqrt{\frac{\sum (\mathrm{x}_i - \mu)^2}{\mathrm{N}}} \tag{7}$$

where Σ means "sum of", x_i is a value in the data set, μ is the mean, and N is the number of data points.

The presented analysis (see Table 1) shows that there are no outlier observations in the dataset for both Test sites. The results for the Test Site I demonstrate that:

(1) The reprojection error values (the factor determining the relative orientation accuracy) do not exceed 0.5 pixels for control and check points. The mean and median values are similar: (mean/median) 0.4/0.4 for control points and 0.4/0.4 for check points, respectively. The range of values (difference between the minimum and maximum value) is 0.1 pixel for control points and 0.2 pixel for check points. The RMSE values for control and check points are equal and are 0.4. The process of the relative orientation of the images was performed correctly, and according to the theory of errors (3 RMSE values), the maximum reprojection error of the point measurement does not exceed 1.2 pixels.

(2) The accuracy analysis of the external orientation of the photos based on deviations for linear values (accuracy of determining the position of a point in 3D) demonstrates that the maximum values do not exceed 3 sigma of the accuracy of determining the position (measurement error was 1.5 mm) and are respectively 4.2 mm for control points and 2.7 mm for check points. This proves the correct external orientation of the images. As in the case of reprojection error, the mean and median values are similar and are 2.7/2.4 mm for control points and 2.2/2.0 for check points, respectively. The maximum linear error of the point measurement does not exceed 4.5 mm – three times the RMSE of determination of the position of the measured point with the total station.

(3) From the analysis of deviations for coordinates X, Y and Z, it can be concluded that the largest errors were obtained for coordinates Y and Z (related to the deviations of point determination in width and height of the surface, instead of deviation to the wall surface). Comparing the obtained values for control and check points, one can see similar values, which proves the correctness of the conducted process of orientation of external images and the lack of outliers in observations.

The results of the deviation analysis on the control and check points on Test Site II show similar correlations to the data obtained for Test Site I.

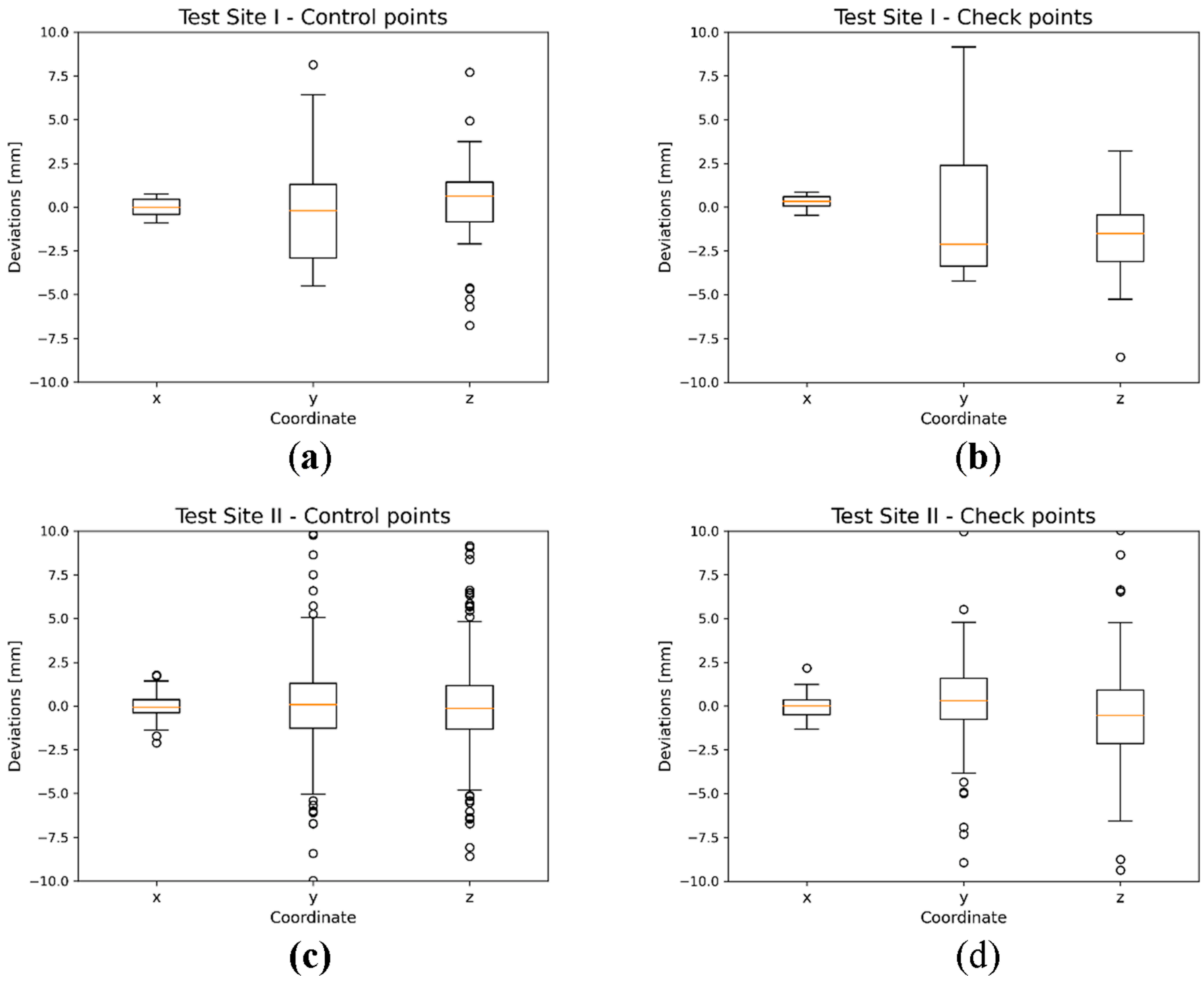

Fig. 9. Box plots for the distribution of the deviations on (a) control points for Test Site I, (b) check points for Test Site I, (c) control points for Test Site II and (d) check points for Test Site II.

(4) The analysis of the reprojection error values shows that the maximum value is 0.6 pixels for control points and 0.7 pixels for check points. The maximum and minimum value difference is 0.5 pixels for control points and 0.2 pixels for check points. The mean and median values for control and check points are similar and are 0.3/0.4 and 0.4/0, respectively.

(5) As in the case of Test Site I, the maximum values of linear deviations do not exceed 3 of the RMSE of determining the position of a 3D point from total station measurements and are 4 mm for control points and 4.4 mm for check points, respectively. This proves the absence of outliers in the data set. The difference between the mean and median value for the control points is 0.3 mm and for the check points 0.5 mm, which confirms the correctness of the bundle adjustment process. The RMSE values are 3.3 mm for the control points and 2.6 mm for the check points, respectively, which confirms the above statement.

(6) In the case of statistical analysis of deviations on control and check points, a similar trend occurs in the case of Test Site I, i.e., larger errors in determining the horizontal and vertical position (on the wall) than in depth (deviations from wall surface).

3.2.2. The TLS- SfM based on the control and check points automatically detected in the TLS point cloud

The relative orientation of point clouds from the terrestrial laser scanner and close-range images based on the point cloud converted into the orthoimages form (with depth maps and GSD 2 mm) and natural points detected by the SURF detector (Fig. 8).

The deviation results were visualised using the boxplots (Fig. 9) due to the higher number of control and check points (Fig. 8) detected on TLS point clouds, when compared to the “classical SfM”.

The analysed TLS results are presented in Fig. 8a and b (Test Site I), demonstrating the deviations of the natural control and check points did not exceed ± 10 mm for X, Y and Z-coordinates.

(1) The median values (orange line) of X deviations for control and check points are equal to 0 mm, the interquartile range (IQR) is approximately equal to 1 mm (grayscale box) and the minimum and maximum values were smaller than ± 2 mm, which proves the lack of systematic errors.

(2) For Y- coordinates deviations, the median values for control and check points are different, and for check points are approximately equal to −2.5 mm. The Q1 and Q3 values for control points are –2.5 mm and 1.5 mm, and for check points are −3.5 mm and 2.5 mm, respectively. The maximum and minimum values are 6.5

mm and −3.5 mm for the control points and 8 mm and −3.5 mm for the check points, respectively. The minimum, maximum, Q1 and Q3 values are not symmetric with respect to the median, indicating systematic errors.

(3) For Z-coordinates deviations, the median value for control points is approximately 0 mm and for check points −2 mm. Comparing the Q1 and Q3 values for Z-coordinates are lower than for Y-coordinates but higher than for X-coordinates and are −1.5 mm and 1.5 mm for control points and −2.5 mm and −1 mm for check points, respectively. For the maximum and minimum values, deviations of −1.5 mm and 3.5 mm were obtained for the control points and −6 mm and 3 mm for the check points. There are no systematic errors for control points.

Similar accuracy analysis was performed for Test Site II (Fig. 8 c,d), where the error values do not exceed ± 10 mm, but unlike the previous Test Site, there are outliers in the dataset (marked as circles on the boxplot).

(1) The distribution of deviations for X-coordinates values is similar to those obtained for Test Site I. The median value is approximately 0, and the IQR is about 1 mm. There is a noticeable difference in the minimum and maximum values, approximately ± 2 mm for control points and ± 1.5 mm for check points, respectively. The distribution of values compared to the median is symmetric, which proves the absence of outliers.
(2) For the Y-coordinate, the distribution of deviations is symmetrical compared to the median (for control and check points), which is approximately 0. The Q1 and Q3 values are ± 1.5 mm, and the minimum and maximum values do not exceed ± 5 mm. The spread of deviations is less than for Test Site I.
(3) The distribution and values on the boxplot for deviations for Z-coordinates are similar to Y-coordinates. For the check points, the median is approximately 1 mm, the Q1 and Q3 are −2.5 mm and 1 mm, respectively, and the minimum and maximum values are 6.5 mm and 4.5 mm. The distribution of values is symmetrical to the median value, but it is not equal to zero, indicating a systematic error.

To summarise, both Test Sites demonstrated small deviation values for the X coordinate, which was directed perpendicular to the plane of the wall. The errors in the direction of the Y and Z coordinates occurred due to the correctness of detection and matching of feature points on the orthoimages. Despite systematic errors (for Test Site I approx. −2.5 mm and Test Site II approx. 0.5 mm), the registration process was carried out correctly, considering the GSD value being 2 mm for both orthoimages.

3.2.3. The comparison of the proposed methods for "base orthoimage" orientation

This study shows that the application of the "classical" SfM method (based on reference points measured in the total station) and the TLS SfM method (based on reference points automatically detected in the point cloud) achieves similar accuracy in the bundle adjustment process. When selecting between these two methods for the orientation of the base images, the following factors should be considered:

(1) Identification of the same reference points in the photos and during total station measurement. The external orientation was made on the natural points of the object (the points were not marked), which often made it difficult for the observer to identify the point in the image. By using the feature-based method, it is possible to detect points on both datasets automatically, and with a larger number of points (compared to the total station measurement method), it is possible to filter out points that do not meet the accuracy requirements while maintaining the correct spatial distribution.

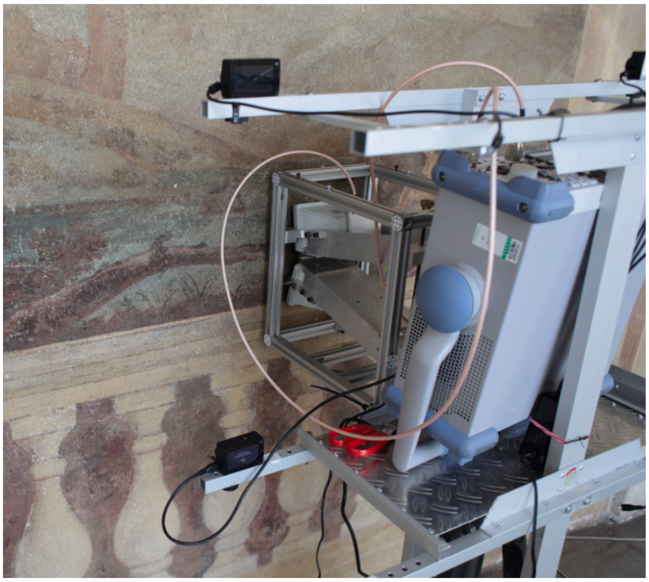

Fig. 10. The example image of a measurement platform system with retroreflective points used to orient horn antennas in a defined reference system.

(2) Time of measurement of reference points. In the case of total station measurements, it is necessary to carry out measurements from at least two different stations in two series to obtain millimetre accuracy and perform the simultaneous control of the measurements. When acquiring point clouds with TLS, the process is fully automatic and does not require points to be manually "pointed out", which significantly impacts data acquisition time.
(3) The proposed TLS SfM method works well for developing objects with varying textures and structures. In the case of white walls without decorations, it is recommended to use a method based on signalled reference points measured by total station.

3.2.4. MW Sensor position determination with the SfM approach

The following data processing step consisted of determining the individual MW system's position using a two-step approach:

(1) Determining the relative orientation of the images (acquired according to Scenario II) with respect to the images processed in the previous step ("base orthoimage").
(2) Determination of the position of antennas (MW signal transmitter and receiver) based on signalled points located in the sensor housing (Fig. 10) and known geometrical relations between them (Fig. 2a).

To perform an independent check of the accuracy of the determination of the signalled points on the MW housing, measurements of the coordinates of the points were made using a total station. These points were used as check points in the bundle adjustment process. The minimum, maximum and mean values of RMSE (Eq.1) were used to evaluate the quality of the image's orientation for the measured wall and each of the MW positions. Additionally, the RMSE and Sigma Median Absolute Deviation (SMAD; Eq. (8)) were compared to determine the presence of outliers in the dataset.

$$\mathrm{SMAD} = 1.4826^{*}\,\mathrm{median}(|x_i - \delta|) \tag{8}$$

where x_i is a value in the data set, and δ is the median of the data set.

Table 1 presents an analysis of the orientation accuracy of the images used to determine individual measuring positions of the MW sensor.

The results shown in Table 2 indicate that the orientation of the images is correct for both Test Sites. Based on the analysis of the values of RMSE reprojection error, none of the indicators exceeds 0.5 pixels.

Table 2
The quality assessment of the images' orientation used for orthoimages generation and MW sensor measuring positions.

Test Site	Parameter	Point type	RMSE reprojection error [pix]	RMSE X [mm]	RMSE Y [mm]	RMSE Z [mm]	RMSE L [mm]
I	Minimum	Check points	0.3	0.5	0.5	1.4	1.9
	Maximum		0.5	2.0	3.8	4.4	4.3
	Mean		0.4	1.2	1.7	1.3	3.0
	Median		0.4	1.3	1.4	1.0	3.0
	RMSE		0.04	0.5	1.1	1.1	0.9
	SMAD		0.02	0.5	1.0	0.8	1.3
Test Site	**Parameter**	**Point type**	**RMSE reprojection error [pix]**	**RMSE X [mm]**	**RMSE Y [mm]**	**RMSE Z [mm]**	**RMSE L [mm]**
II	Minimum	Check points	0.3	0.7	0.3	0.5	1.1
	Maximum		0.5	1.3	1.6	1.8	2.4
	Mean		0.4	1.0	0.8	1.0	1.7
	Median		0.4	1.0	0.7	0.9	1.8
	RMSE		0.05	0.2	0.4	0.4	0.5
	SMAD		0.03	0.2	0.5	0.3	0.6

The mean and median of RMSE error are similar for both Test Sites – 0.4 pixels. The standard deviation (RMSE) and SMAD are similar for both Test Sites. The maximum and minimum reprojection errors are between 0.3 and 0.5 pixels for both Test Sites. This indicates the absence of outliers on the control points used for the external orientation of the images.

The accuracy of the external orientation of the images used to generate orthoimages for both Test Sites varies. The linear error of the median values is 3.0 mm for Test Site I, and 1.8 mm for Test Site II. For Test Site I, the median and mean values are similar for all coordinates, with differences of 0.1 mm for the X, 0.3 mm for the Y and 0.3 mm for the Z coordinate on check points. Differences between RMSE and SMAD values less or equal to 0.3 mm can be observed, and this proves that the images orientation is correct in the adopted reference system and that the proposed method of MW sensor position in space allows for accurate localisation determination. It should also be mentioned that the values of errors in determining the exterior orientation do not exceed 4.3 mm for a maximum value and are three times lower than the RMSE of determining the position of the measured point with the total station (4.5 mm). For Test Site II, a similar trend might be seen, but only the maximum value of the RMSE for linear deviation is about 1.8 times lower, which proves the correctness of the orientation process and the absence of outliers in the data set.

Relative errors of the averaged RMSE were set based on the antenna's dimensions and the distance between the antenna and the measured object:

(1) the accuracy of determining the horizontal centre of the antenna was 1.4 % of the width for Test Site I and 1.5 % for Test Site II, respectively;
(2) the accuracy of determining the vertical centre of the antenna was 0.7 % for Test Site I and 1.2 % for Test Site II;
(3) The maximum error (3 times the mean value) for the determination of horizontal position was 4.3 % for Test Site I and 4.5 % for Test Site II.
(4) The maximum error (3 times the average value) for the vertical position was 2.0 % for Test Site I and 3.5 % for Test Site II;
(5) The mean RMSE of determining the distance of the antenna from the wall (X coordinate) was 1.2 mm for Test Site I and 1.0 mm for Test Site II, respectively. This error value will not significantly affect the correction of the MW signal passing through the air, which is a different medium from the wall.

3.3. *Moisture meter analysis*

The yearly moisture content data was recorded using a pin-type moisture meter between the 2nd of October 2018 and the 6th of August 2019. According to Gann [48], the selected pin-type moisture

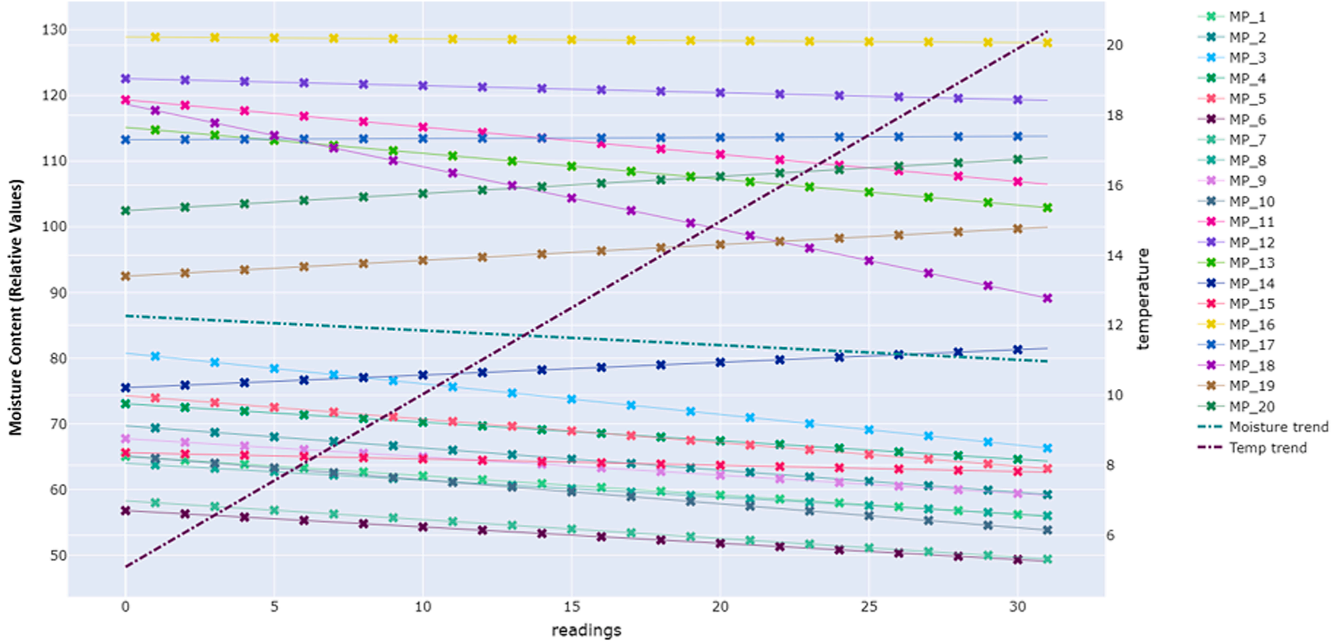

Fig. 11. Yearly moisture meter data (relative values) with the linear moisture and temperature (^{o}C) trends for Test Site I.

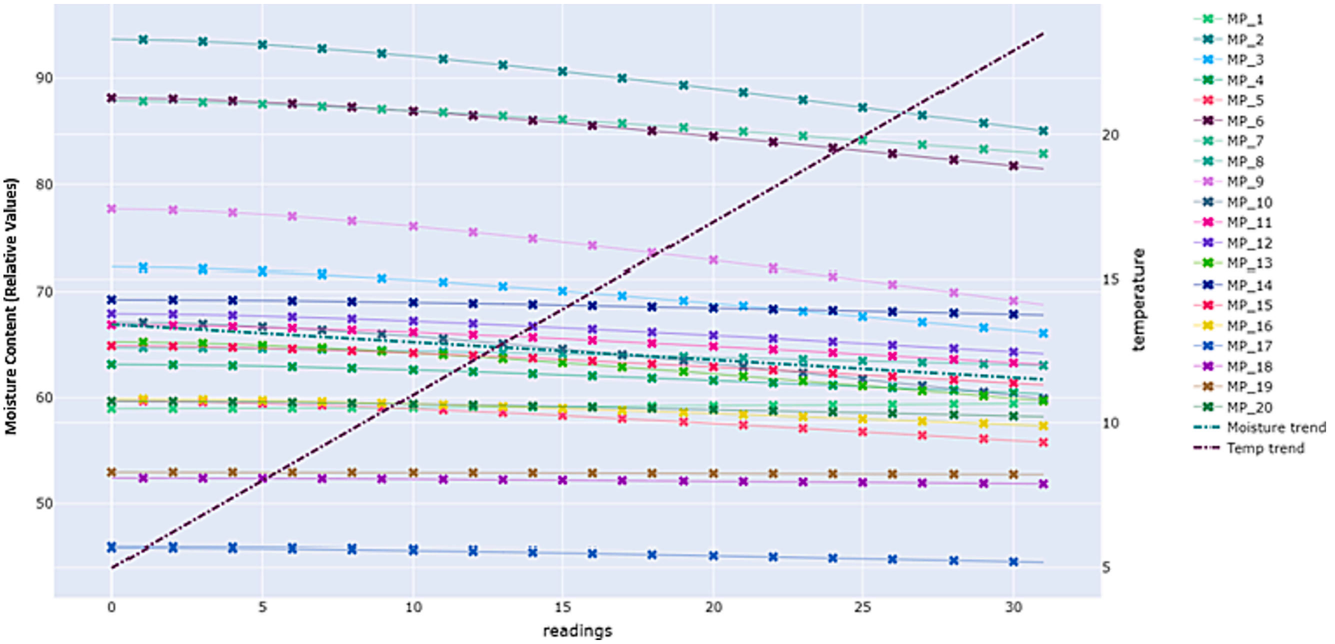

Fig. 12. Yearly moisture meter data (relative values) with the linear moisture and temperature (^{o}C) trends for Test Site II.

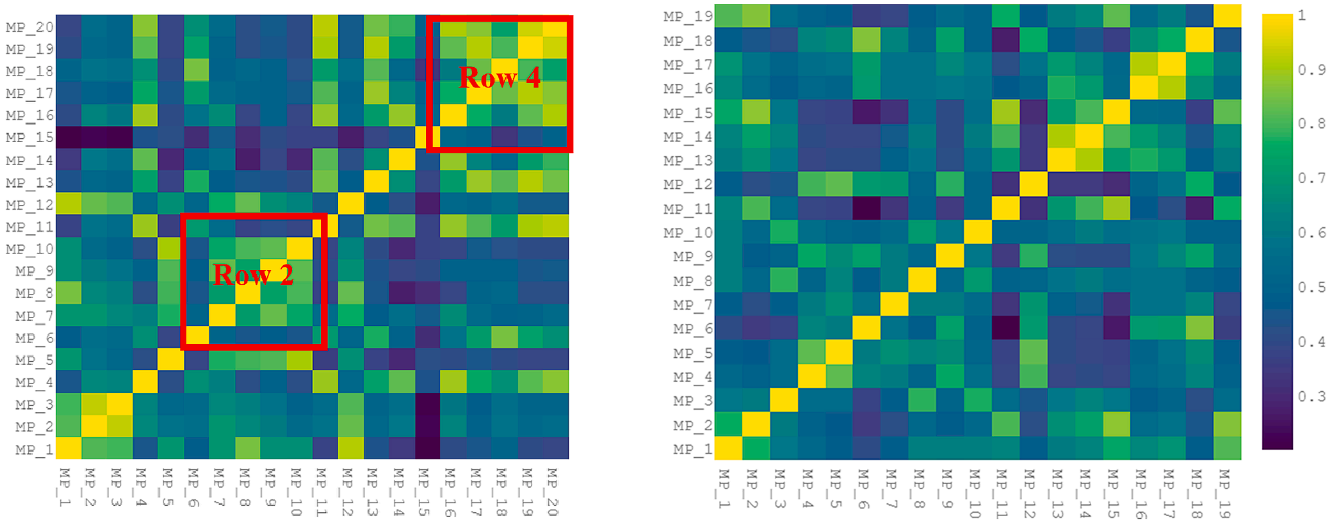

(a)

(b)

Fig. 13. Correlation Heatmap of Moisture data for (a) Test Site I and (b) Test Site II.

meter with active electrode B50 provides the measuring range 0.3–8.5 % moisture content, which is displayed on the moisture meter in relative values ranging from 0 to 199, which can be categorised into 6 groups, namely very dry (20–40)- <1.3 % moisture in weight percent, normal dry (40–60)- 1.3–1.9 % moisture in weight percent, semi-dry (60–80) – 1.9–3.2 % moisture in weight percent, moist (80–100)- 3.2–4.4 % moisture in weight percent, very moist (110–130)- 5–6.2 % moisture in weight percent and wet (above 130)- >6.2 % moisture in weight percent based on the density of historic brick masonry wall [49]. The conservators from the Museum of King Jan III's Palace at Wilanów further combined the categories into 3 groups, namely (1) accepted range of the moisture content for the measured walls (30 and 60), (2) inspection required (61–100) and (3) high-risk moisture level (above 100). During this period, 31 measurements were taken for every measuring position (MP). The indoor and outdoor temperature data was captured in parallel with the moisture measurements. The moisture data shows a decreasing trend over time, whereas the indoor and outdoor temperature shows an increasing trend. Therefore, it can be observed that there is a negative relationship between both measured variables, i.e., the moisture content (relative values of the moisture meter) and the temperature (^{o}C). The moisture meter and temperature trend lines for Test Site I and Test Site II are shown in Fig. 11 and Fig. 12, respectively.

The heatmap of moisture data for Test Site I and Test Site II is presented in Fig. 13a and b, respectively. The heatmap demonstrates that the measuring positions (MPs) in individual rows show a degree of correlation between each other. In Fig. 13a, the red highlighted boxes named rows 2 and 4 show a higher correlation between individual points, suggesting that the moisture content is persistent across these rows. However, there is a weaker correlation between Row 2 and 4. Additionally, the correlation decreases from the first row to the last row in Fig. 13a. This is evident from the analysis of the heatmap that the last row shows higher amount of moisture content as compared to the top

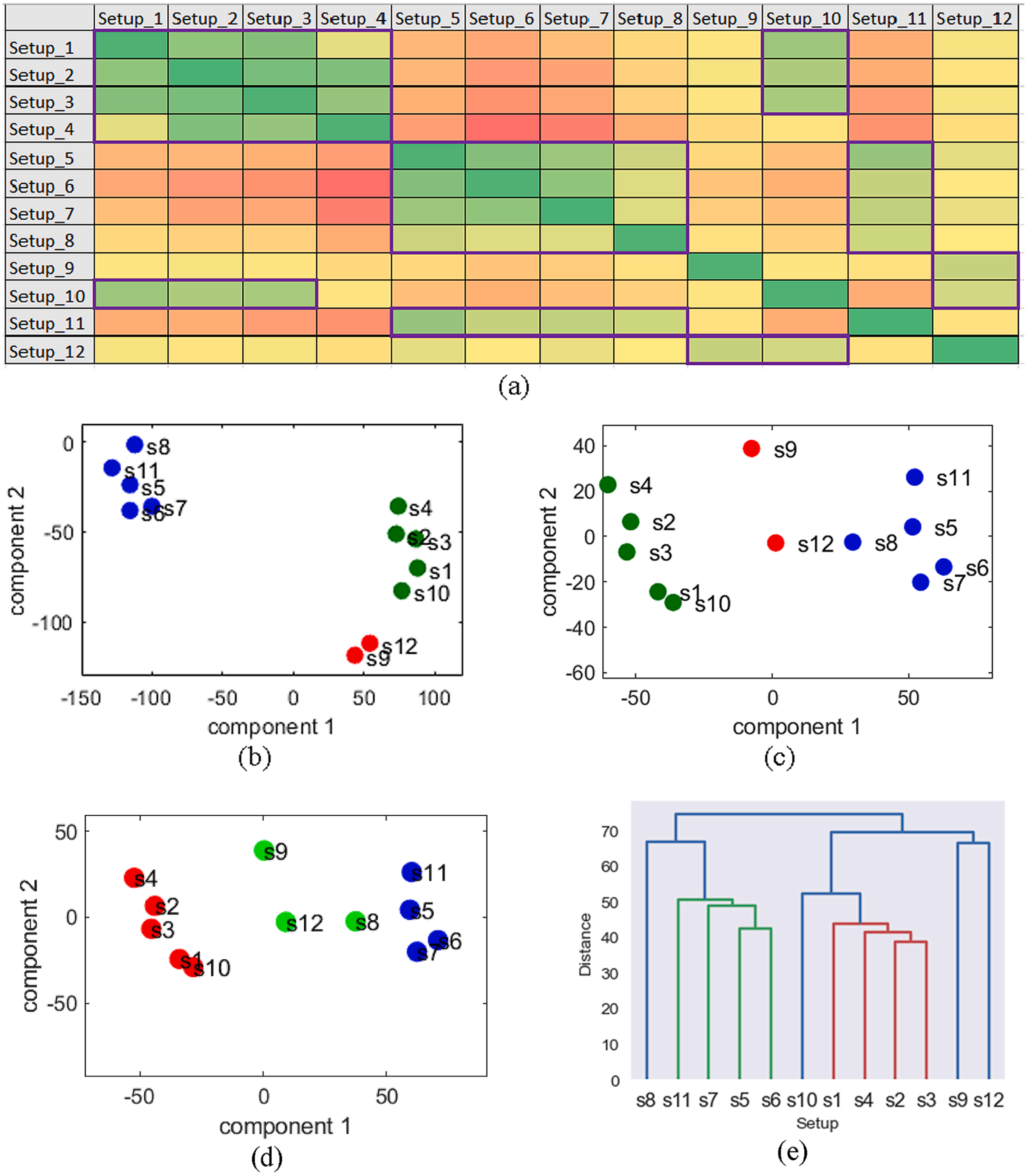

Fig. 14. Data analysis of MW System for water content detection using (a) Correlation heatmap, (b) *t*-SNE, (c) PCA, (d) K-Means, and (e) Hierarchical Clustering for laboratory-based brick setup.

rows in Fig. 13. Furthermore, the MPs in the middle of the rows show higher similarity than the corner MPs, which show less correlation as highlighted in red box Row 2. In Fig. 13b, the amount of moisture varies in the individual rows from left to right, which suggests that there is higher amount of moisture in the last column on the right.

3.4. MW system's data analysis

The initial analysis was carried out on the laboratory-based brick setup to investigate how the presence and location of water interact with the MW spectrum. The correlation heatmap was created (Fig. 14a) for all 12 setups described in the methodology section (Fig. 3). The results of the heatmap outline that there are three groups in the dataset. The first group comprises of setups 1–4 and 10 – the first four setups didn't have any water samples in front of the horn antenna, and the setup 10 didn't have any water samples in the first two rows, i.e. in front of the horn antenna. Thus, there is a strong correlation between these datasets. On the other hand, the setup 4 didn't correlate as strong with setups 1 and 10 compared to setups 2 and 3. This is due to the setup 4 having water samples on the right and left side of the brick, i.e., setups 2 and 3 had water samples on the right and the left side of the brick, respectively. Therefore, the setup 4 had a stronger linear correlation with setups 2 and 3. The second group of datasets included setups 5, 6, 7, 8 and 11 – all these setups had water samples right in front of the horn antenna, namely in the closest/first row. The last group of datasets consisted of setups 9 and 12. These two setups differed from others by having water samples on the second (the setup 9) or second and third rows (the setup 12). The data were further analysed using four clustering techniques, namely (1) *t*-SNE, (2) PCA, (3) K-Means, and (4) Hierarchical Clustering. All four clustering methods were able to categorise the data into three

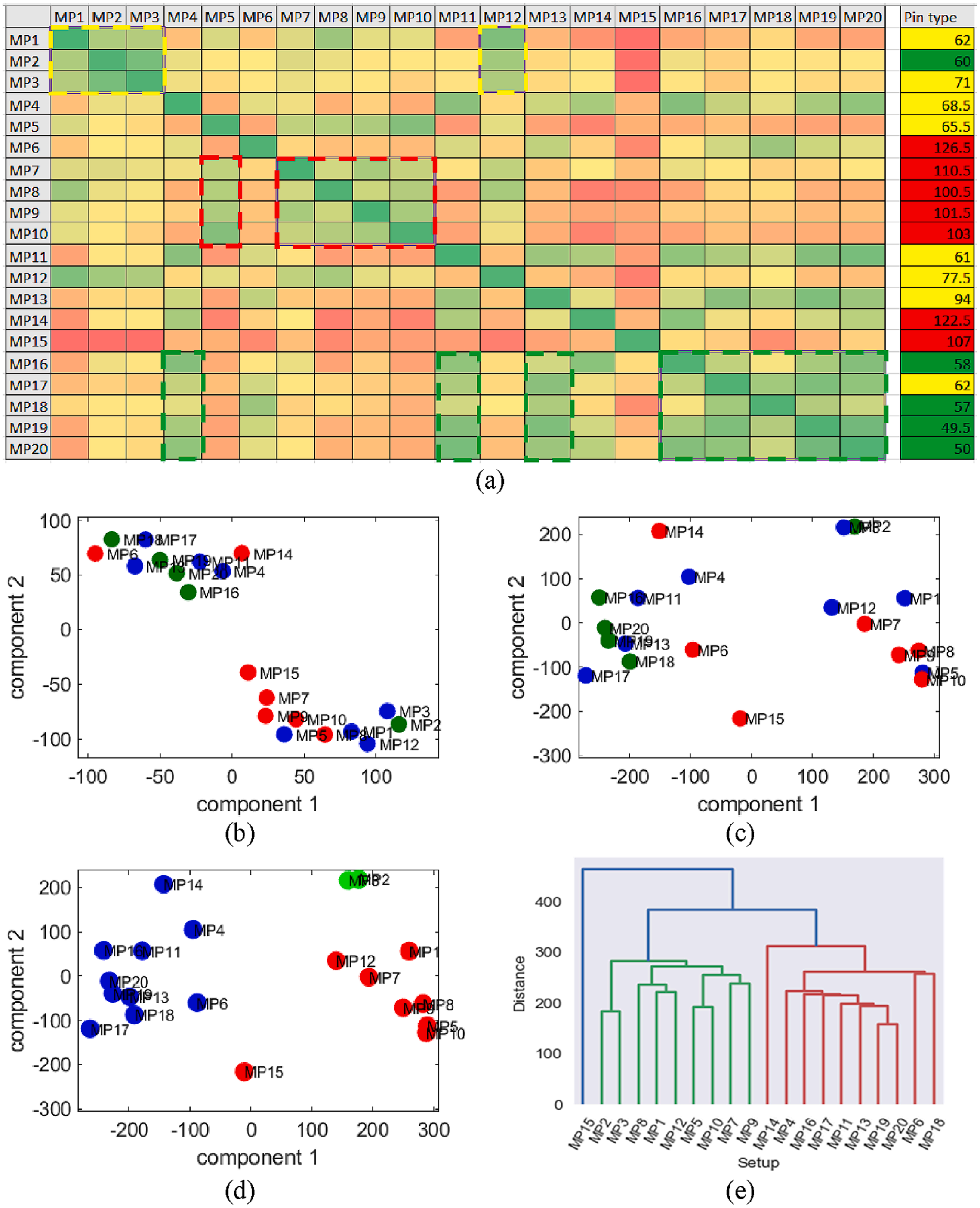

(a)

(b)

(c)

(d)

(e)

Fig. 15. Data analysis of MW System for moisture detection using (a) Correlation heatmap, (b) *t*-SNE, (c) PCA, (d) K-Means, and (e) Hierarchical Clustering for case study Test Site I setup.

groups (see Fig. 14), which aligns with heatmap correlations. This experimental study demonstrated that the MW system is able to identify both the presence and location of water content within the building material, whereas the pin-type moisture measurement method only determines the moisture content on the surface of the building material. This means that the latter method will not provide the true moisture measurement of the building material. Therefore, the MW system is believed to provide in-depth moisture measurement of the building material.

A similar approach (heatmap and clustering techniques) was applied to the MW data obtained in Test Site I and II at the Museum of King Jan III's Palace in Wilanów. The data from Test Site I and Test Site II are presented in Fig. 15 and Fig. 16, respectively. The correlation heatmap of the data (see Fig. 15a for Test Site I and Fig. 16a for Test Site II) demonstrates various groups, which are highlighted with boxes in green, yellow and red colours based on the pin-type moisture meter measurements that are also provided on the right side of the graph. The majority of MW grouped data can be aligned with the pin-type moisture meter data. However, there are individual positions where the MW data do not correlate with the pin-type moisture meter data. This could be caused by the different moisture content on the surface and inside the measured wall, i.e., the MW system is able to penetrate through the measured wall

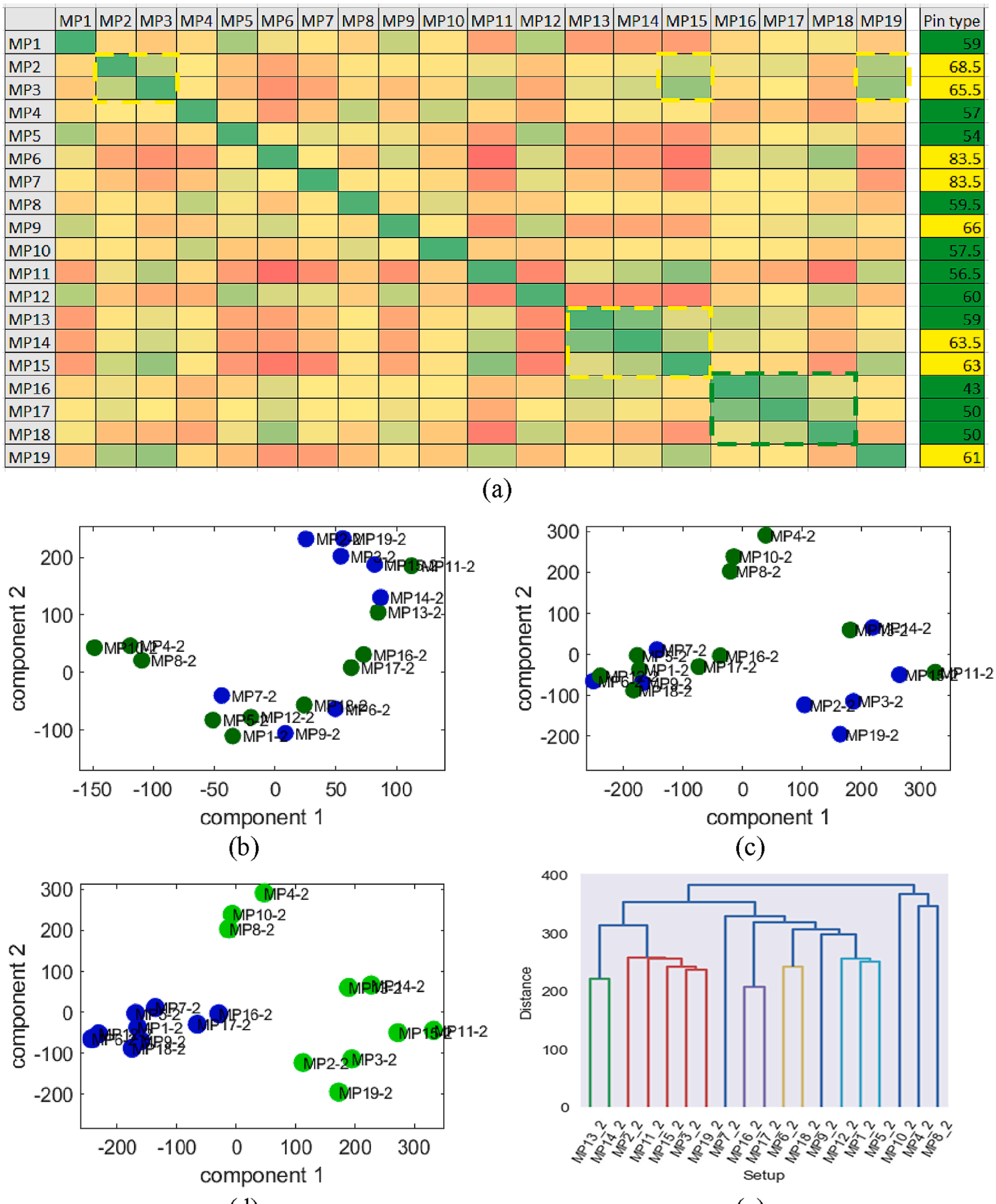

(a)

(b)

(c)

(d)

(e)

Fig. 16. Data analysis of MW System for moisture detection using (a) Correlation heatmap, (b) *t*-SNE, (c) PCA, (d) K-Means, and (e) Hierarchical Clustering for case study Test Site II setup.

and determine the presence and location of moisture within the wall, which can be confirmed by the undertaken laboratory study on the brick experimental setup. Further analysis was carried out using the same clustering techniques used in the brick experimental setup, namely (1) *t*-SNE, (2) PCA, (3) K-Means and (4) Hierarchical Clustering, which are presented in Fig. 15 and Fig. 16 for Test Site I and Test Site II, respectively. The clustering for Test Site I was set to determine three clusters in the data based on the pin-type moisture meter data (three thresholds for moisture content). The K-Means method was able to clearly identify-three clusters in the data, whereas the *t*-NSE and PCA results provided overlapping clusters. The Hierarchical technique identified two main groups and numerous sub-groups. Furthermore, all the methods identified one outlier in the results, namely “MP15”, which can also be observed in the correlation heatmap (see Fig. 15a). The potential reason for this outlier is thought to be a foreign object’s presence inside the wall. Performed clustering analysis demonstrated that the MW system’s data does not fully align with the pin-type moisture meter data as it was expected due to the penetration capability and influence of the presence and location of moisture within the wall on the MW signal. The precise quantitative measurement of moisture inside the measured wall is impossible due to the use of destructive methods. However, the MW system demonstrated the ability to estimate the moisture presence and its location inside a wall structure.

4. Conclusion

The cultural heritage sites face day-to-day challenges with the extreme weather conditions (environmental change) and the assessment processes due to current limitations of utilised techniques. One of the most crucial monitoring parameters in cultural heritage is moisture content owing to the severity of caused damages to the sites. Thus, the research and development of adequate and appropriate monitoring techniques for excess moisture in cultural heritage sites are highly important. This article presented a novel approach based on the deep-penetration microwave technique complemented by the geo-positioning method using photogrammetry and terrestrial laser scanners. Previously, several studies were undertaken using microwave spectroscopy, which lacked the geo-positioning capability of the system that is essential in identifying the measuring positions for architectural documentation. The proposed methodology was experimentally studied at the Museum of King Jan III's Palace at Wilanów, Poland, which suffers from excess moisture content on frescoes from the XVII century. Currently, the excess moisture in this museum is monitored using a pin-type moisture meter, which only provides surface measurements of walls/paintings, and the data is captured and recorded manually. The moisture data from the pin type meter demonstrated that the lower sections of the measured walls had higher moisture content and a negative correlation against temperature data. This can be explained by the impact of the high temperatures on the drying process of the walls. The experimental work was undertaken using the proposed microwave sensing approach combined with the photogrammetry and terrestrial laser scanner to study the progression of moisture within the walls. The photogrammetry and terrestrial laser scanner were initially used to geolocalise the microwave sensing system in space (on the frescoes) and to develop multispectral architectural documentation required for safeguarding and preservation of cultural heritage buildings. The microwave data were processed and analysed using *t*-SNE, PCA, K-Means and Hierarchical clustering algorithms to identify groups within the data. The microwave system demonstrated a weak correlation against the pin-type moisture meter data. This is due to the measuring approach of each technique, i.e., the microwaves are able to penetrate through the material, whereas the pin-type meter only measures the surface of the material. Therefore, it could be assumed that the microwave sensing approach provides more detailed moisture information of the measured walls.

Future work can involve the optimisation of the proposed system, namely, to minimise the dimensions and cost of the platform, namely (1) develop a built-in RF circuitry (to replace VNA), (2) implement a built-in camera for a portable all-in-one handheld system and (3) explore different types of antennas (e.g. microstrip/patch type antennas). Further data could be collected from numerous moisture measuring positions and frescoes to evaluate the current state of the measured gallery. Furthermore, a prediction model using machine learning algorithms should be developed to provide an early warning for sustainable preservation and safeguarding of cultural heritage. The system can also be tested and evaluated on different absorbent building materials, namely timber, stones and concrete, at various historical sites.

Author Contributions

M.M., J.M., and P.K. organised the conceptualisation of the idea and the methodology employed in this paper. Following that, J.M., A.T., S. Ł., M.M. and K.O. carried out the experimental design. P.K., J.M., A.T., K.O. and S.Ł., worked on the data acquisition at the Museum of King Jan III's Palace at Wilanów. M.M, P.K. J.M. and S.Ł carried out the original writing and draft preparation. J.M., G.M. and K.H undertook the data analysis. A.S. and D.Z carried out the review and the editing. All authors have read and agreed to the published version of the manuscript.

Funding

The program is co-financed by the European Social Fund under the Operational Program Knowledge Education Development, a non-competition project entitled “International scholarship exchange of doctoral students and academic staff” implemented as part of the Activity specified in the application for co-financing of the project no. POWR.03.03.00–00-PN13 / 18. The research was funded by the Warsaw University of Technology within the Excellence Initiative: Research University (IDUB) programme (No. 1820/55/Z01/2021).

Declaration of Competing Interest

The authors declare the following financial interests/personal relationships which may be considered as potential competing interests: [Professor Patryk Kot reports financial support was provided by European Social Fund. Dr Jakub Markiewicz reports financial support was provided by Warsaw University of Technology.].

Data availability

The authors are unable or have chosen not to specify which data has been used.

References

[1] P. Kot, K. Hashim, M. Muradov, R. Al Khaddar, How can sensors be used for sustainability improvement? in: R. Jingzheng (Ed.), Methods Sustain. Sci. (Assessment, Prioritisation, Improv. Des. Optim., Elsevier, 2021: pp. 321–344.

[2] A. Llorente-Alvarez, M.S. Camino-Olea, A. Cabeza-Prieto, M.P. Saez-Perez, M. A. Rodríguez-Esteban, The thermal conductivity of the masonry of handmade brick Cultural Heritage with respect to density and humidity, J. Cult. Herit. 53 (2022) 212–219, https://doi.org/10.1016/j.culher.2021.12.004.

[3] European Framework for Action on Cultural Heritage, Office of the European Union, Luxembourg, 2019. http://openarchive.icomos.org/id/eprint/2317/.

[4] A. Blyth, R. Napolitano, B. Glisic, Documentation, structural health monitoring and numerical modelling for damage assessment of the Morris Island Lighthouse, Philos. Trans. R. Soc. A Math. Phys. Eng. Sci. 377 (2019) 20190002, https://doi.org/10.1098/rsta.2019.0002.

[5] L.M. Gandham, J.R. Kota, P. Kalapatapu, V.D.K. Pasupuleti, A Survey on Current Heritage Structural Health Monitoring Practices Around the Globe, in: 2021: pp. 565–576. https://doi.org/10.1007/978-3-030-73043-7_48.

[6] F. Clementi, A. Formisano, G. Milani, F. Ubertini, Structural health monitoring of architectural heritage: from the past to the future advances, Int. J. Archit. Herit. 15 (2021) 1–4, https://doi.org/10.1080/15583058.2021.1879499.

[7] M. Wojtkowska, M. Kedzierski, P. Delis, Validation of terrestrial laser scanning and artificial intelligence for measuring deformations of cultural heritage structures, Measurement. 167 (2021), 108291, https://doi.org/10.1016/j.measurement.2020.108291.

[8] J. Markiewicz, M. Pilarska, S. Łapiński, A. Kaliszewska, R. Bieńkowski, A. Cena, Quality assessment of the use of a medium format camera in the investigation of wall paintings: an image-based approach, Meas. J. Int. Meas. Confed. 132 (2019) 224–237, https://doi.org/10.1016/j.measurement.2018.07.001.

[9] S. Peña-Villasenín, M. Gil-Docampo, J. Ortiz-Sanz, Desktop vs cloud computing software for 3D measurement of building façades: the monastery of San Martín Pinario, Measurement. 149 (2020), 106984, https://doi.org/10.1016/j.measurement.2019.106984.

[10] C. Wu, Y. Yuan, Y. Tang, B. Tian, Application of Terrestrial Laser Scanning (TLS) in the Architecture, Engineering and Construction (AEC) Industry, Sensors. 22 (2021) 265, https://doi.org/10.3390/s22010265.

[11] Lu-Xingchang, Liu-Xianlin, Reconstruction of 3D Model Based on Laser Scanning, in: Innov. 3D Geo Inf. Syst., Springer, Berlin, Heidelberg, Berlin, Heidelberg, 2006: pp. 317–332. https://doi.org/10.1007/978-3-540-36998-1_25.

[12] D. Pritchard, J. Sperner, S. Hoepner, R. Tenschert, Terrestrial laser scanning for heritage conservation: The Cologne Cathedral documentation project, in: ISPRS Ann. Photogramm. Remote Sens. Spat. Inf. Sci. 28 August–01 Sept. 2017, Ottawa, Ottawa, Canada, 2017: pp. 213–220. https://doi.org/10.5194/isprs-annals-IV-2-W2-213-2017.

[13] M. Ricciardi, C. Pironti, O. Motta, R. Fiorillo, F. Camin, A. Faggiano, A. Proto, Investigations on historical monuments' deterioration through chemical and isotopic analyses: an Italian case study, Environ. Sci. Pollut. Res. 29 (2022) 29409–29418, https://doi.org/10.1007/s11356-021-15103-x.

[14] I. Garrido, S. Lagüela, S. Sfarra, P. Arias, Development of thermal principles for the automation of the thermographic monitoring of cultural heritage, Sensors. 20 (2020) 3392, https://doi.org/10.3390/s20123392.

[15] A. Sardella, E. Palazzi, J. von Hardenberg, C. Del Grande, P. De Nuntiis, C. Sabbioni, A. Bonazza, Risk mapping for the sustainable protection of cultural

heritage in extreme changing environments, Atmosphere (Basel). 11 (2020) 700, https://doi.org/10.3390/atmos11070700.

[16] M. Bacci, A. Casini, M. Picollo, B. Radicati, L. Stefani, Integrated non-invasive technologies for the diagnosis and conservation of the cultural heritage, J. Neutron Res. 14 (2006) 11–16, https://doi.org/10.1080/10238160600672930.

[17] E. Sesana, A. Gagnon, C. Bertolin, J. Hughes, Adapting cultural heritage to climate change risks: perspectives of cultural heritage experts in Europe, Geosciences. 8 (2018) 305, https://doi.org/10.3390/geosciences8080305.

[18] S. Ramírez, M. Zarzo, A. Perles, F.-J. García-Diego, A methodology for discriminant time series analysis applied to microclimate monitoring of fresco paintings, Sensors 21 (2021) 436, https://doi.org/10.3390/s21020436.

[19] T. Rymarczyk, G. Kłosowski, A. Hoła, J. Hoła, J. Sikora, P. Tchórzewski, Ł. Skowron, Historical buildings dampness analysis using electrical tomography and machine learning algorithms, Energies 14 (2021) 1307, https://doi.org/10.3390/en14051307.

[20] E. Rosina, A. Sansonetti, N. Ludwig, Moisture: The problem that any conservator faced in his professional life, J. Cult. Herit. 31 (2018) S1–S2, https://doi.org/10.1016/j.culher.2018.04.022.

[21] M. Giuliano, C. Manzo, Spectral response of architectural surface as support to analyses of materials and degradation, Preserv. Conserv. Cult. Herit. (2014) 579–590.

[22] P. Kot, M. Muradov, M. Gkantou, G.S. Kamaris, K. Hashim, D. Yeboah, Recent advancements in non-destructive testing techniques for structural health monitoring, Appl. Sci. 11 (2021) 2750, https://doi.org/10.3390/app11062750.

[23] M.I. Martínez-Garrido, R. Fort, M. Gómez-Heras, J. Valles-Iriso, M.J. Varas-Muriel, A comprehensive study for moisture control in cultural heritage using non-destructive techniques, J. Appl. Geophys. 155 (2018) 36–52, https://doi.org/10.1016/j.jappgeo.2018.03.008.

[24] Protimeter, SurveyMaster, SurveyMaster. (n.d.). https://www.protimeter.com/surveymaster.

[25] J.K. Delaney, J.G. Zeibel, M. Thoury, R. Littleton, M. Palmer, K.M. Morales, E.R. De La Rie, A. Hoenigswald, Visible and infrared imaging spectroscopy of picasso's harlequin musician: mapping and identification of artist materials in situ, Appl. Spectrosc. 64 (2010) 584–594, https://doi.org/10.1366/000370210791414443.

[26] M.C. Di Tuccio, N. Ludwig, M. Gargano, A. Bernardi, Thermographic inspection of cracks in the mixed materials statue: Ratto delle Sabine, Herit. Sci. 3 (2015), https://doi.org/10.1186/s40494-015-0041-6.

[27] F. Fischanger, G. Catanzariti, C. Comina, L. Sambuelli, G. Morelli, F. Barsuglia, A. Ellaithy, F. Porcelli, Geophysical anomalies detected by electrical resistivity tomography in the area surrounding Tutankhamun's tomb, J. Cult. Herit. 36 (2019) 63–71, https://doi.org/10.1016/j.culher.2018.07.011.

[28] C.-H.-M. Tso, O. Kuras, P.B. Wilkinson, S. Uhlemann, J.E. Chambers, P.I. Meldrum, J. Graham, E.F. Sherlock, A. Binley, Improved characterisation and modelling of measurement errors in electrical resistivity tomography (ERT) surveys, J. Appl. Geophys. 146 (2017) 103–119, https://doi.org/10.1016/j.jappgeo.2017.09.009.

[29] O. Sass, H.A. Viles, How wet are these walls? Testing a novel technique for measuring moisture in ruined walls, J. Cult. Herit. 7 (2006) 257–263, https://doi.org/10.1016/j.culher.2006.08.001.

[30] T. Klewe, C. Strangfeld, S. Kruschwitz, Review of moisture measurements in civil engineering with ground penetrating radar – Applied methods and signal features, Constr. Build. Mater. 278 (2021), 122250, https://doi.org/10.1016/j.conbuildmat.2021.122250.

[31] M.K. Wutke, Use of Ground Penetrating Radar measurement combined to resistivity measurement for characterisation of the concrete moisture, 17th Int. Conf. Gr Penetrating Radar, IEEE 2018 (2018) 1–7, https://doi.org/10.1109/ICGPR.2018.8441577.

[32] L. D'Alvia, E. Pittella, E. Rizzuto, E. Piuzzi, Z. Del Prete, A portable low-cost reflectometric setup for moisture measurement in cultural heritage masonry unit, Measurement 189 (2022), 110438, https://doi.org/10.1016/j.measurement.2021.110438.

[33] S.A. Orr, L. Fusade, M. Young, D. Stelfox, A. Leslie, J. Curran, H. Viles, Moisture monitoring of stone masonry: a comparison of microwave and radar on a granite wall and a sandstone tower, J. Cult. Herit. 41 (2020) 61–73, https://doi.org/10.1016/j.culher.2019.07.011.

[34] P. Kot, A. Shaw, M. Riley, A.S. Ali, A. Cotgrave, The feasibility of using electromagnetic waves in determining membrane failure through concrete, Int. J. Civ. Eng. 15 (2017) 355–362, https://doi.org/10.1007/s40999-016-0074-6.

[35] P. Kot, A.S. Ali, A. Shaw, M. Riley, A. Alias, The application of electromagnetic waves in monitoring water infiltration on concrete flat roof: the case of Malaysia, Constr. Build. Mater. 122 (2016) 435–445, https://doi.org/10.1016/j.conbuildmat.2016.06.092.

[36] H. Güneyli, S. Karahan, A. Güneyli, N. Yapıcı, Water content and temperature effect on ultrasonic pulse velocity of concrete, Russ. J. Nondestruct. Test. 532 (53) (2017) 159–166, https://doi.org/10.1134/S1061830917020024.

[37] A. Tobiasz, J. Markiewicz, S. Łapiński, J. Nikel, P. Kot, M. Muradov, Review of methods for documentation, management, and sustainability of cultural heritage case study: museum of King Jan III's Palace at Wilanów, Sustainability. 11 (24) (2019) 7046, https://doi.org/10.3390/su11247046.

[38] J. Markiewicz, S. Łapiński, P. Kot, A. Tobiasz, M. Muradov, J. Nikel, A. Shaw, A. Al-Shamma'a, The quality assessment of different geolocalisation methods for a sensor system to monitor structural health of monumental objects, Sensors (Switzerland) 20 (10) (2020) 2915.

[39] S. Okamura, Microwave Technology for Moisture Measurement, Subsurf. Sens. Technol. Appl. 1 (2000) 205–227, https://doi.org/10.1023/A:1010120826266.

[40] S. Kim, J. Surek, J. Baker-Jarvis, Electromagnetic metrology on concrete and corrosion, J. Res. Natl. Inst. Stand. Technol. 116 (2011) 655, https://doi.org/10.6028/jres.116.011.

[41] S. Pisa, E. Pittella, E. Piuzzi, P. D'Atanasio, A. Zambotti, "Permittivity measurement on construction materials through free space method, in: I2MTC 2017 - 2017 IEEE Int. Instrum. Meas. Technol. Conf. Proc., pp. 11–14, 2017, doi: 10.1109/I2MTC.2017.7969867.

[42] Steatite Ltd (Antennas), Wideband Horn Antenna, (2019) https://www.steatite-antennas.co.uk/wp-content/uploads/2019/01/QWH-SL-2-18-S-SG-R.pdf.

[43] G. Omer, P. Kot, W. Atherton, M. Muradov, M. Gkantou, A. Shaw, M. Riley, K. Hashim, A. Al-Shamma'a, A non-destructive electromagnetic sensing technique to determine chloride level in maritime concrete, Karbala Int. J. Mod. Sci. 7 (1) (2021).

[44] Agisoft, Agisoft Metashape, (2021). https://www.agisoft.com/.

[45] W. Fang, X. Huang, F. Zhang, D. Li, Intensity correction of terrestrial laser scanning data by estimating laser transmission function, IEEE Trans. Geosci. Remote Sens. 53 (2015) 942–951, https://doi.org/10.1109/TGRS.2014.2330852.

[46] J. Markiewicz, P. Podlasiak, D. Zawieska, A new approach to the generation of orthoimages of cultural heritage objects-integrating TLS and image data, Remote Sens. 7 (12) (2015) 16963–16985.

[47] H. Bay, T. Tuytelaars, L. Van Gool, SURF: Speeded up robust features, Lect. Notes Comput. Sci. (Including Subser. Lect. Notes Artif. Intell. Lect. Notes Bioinformatics) 3951 (2006) 404–417, https://doi.org/10.1007/11744023_32.

[48] GANN, "Gann Hydromette Uni 1 + Uni 2," 2001, [Online]. Available: https://www.gann.de/_Resources/Persistent/f108529c9e130dc739403b303170bb20b7d54d88/UNI1_UNI2_EN.pdf.

[49] M.A. Rodríguez-Esteban, M.S. Camino-Olea, A. Llorente-Álvarez, A. Cabeza-Prieto, M.P. Sáez-Pérez, Brick of the historical heritage: comparative analysis of the thermal conductivity, density and moisture, IOP Conf. Ser. Mater. Sci. Eng. 1203 (3) (2021), 032042, https://doi.org/10.1088/1757-899x/1203/3/032042.